Nanoscale

PAPER

Cite this: *Nanoscale*, 2019, **11**, 7149

Morphological and crystallographic orientation of hematite spindles in an applied magnetic field†

Dominika Zákutná, [a,b] Yannic Falke,[b] Dominique Dresen,[b] Sylvain Prévost, ‡[c] Philipp Bender, [d] Dirk Honecker [a] and Sabrina Disch *[b]

Received 27th November 2018,
Accepted 31st January 2019

DOI: 10.1039/c8nr09583c

rsc.li/nanoscale

The magnetic response of spindle-shaped hematite (α-Fe_2O_3) nanoparticles was investigated by simultaneous small-angle and wide-angle X-ray scattering (SAXS/WAXS) experiments. The field-dependent magnetic and nematic order parameters of the magnetic single-domain nanospindles in a static magnetic field are fully described by SAXS simulations of an oriented ellipsoid with the implemented Langevin function. The experimental scattering intensities of the spindle-like particles can be modeled simply by using the geometrical (length, radius, size distribution) and magnetic parameters (strength of magnetic field, magnetic moment) obtained from isotropic SAXS and macroscopic magnetization measurements, respectively. Whereas SAXS gives information on the morphological particle orientation in the applied field, WAXS texture analysis elucidates the atomic scale orientation of the magnetic easy direction in the hematite crystal structure. Our results strongly suggest the tendency for uniaxial anisotropy but indicate significant thermal fluctuations of the particle moments within the hematite basal plane.

1 Introduction

The response of magnetic nanoparticles (NPs) to applied static and dynamic magnetic fields has tremendous technological importance, *e.g.* for medical applications[1] in imaging[2] and magnetic hyperthermia,[3] sensor applications,[4,5] and nanorheology.[6–8] Anisometric NP shapes, such as rods and wires, introduce additional complexity by their reorientation behavior resulting in new phenomena with modified properties. At a high volume fraction, anisometric particles readily self-organize into liquid crystalline arrangements with a nematic–isotropic phase transition as observed for the rod-like tobacco mosaic virus.[9] Self-organization of shape anisotropic NPs into oriented arrangements can further be directed by electric or magnetic fields[10,11] as well as shear flow[12,13] resulting in materials with anisotropic physical properties.

The combination of anisometric shape with uniaxial magnetism leads to different reorientation characteristics depending on the relative orientation of the structural principal axis and magnetization. As a result of dominant shape anisotropy, elongated magnetic particles such as nickel nanorods,[8,14,15] $Co_xFe_{3-x}O_4$ nanowires,[16] or iron oxide nanotubes[17] are mostly magnetized along their principal axis. However, due to inhomogeneous demagnetizing fields, multidomain structures, and the related complex magnetization reversal including the formation of vortices, the orientation of magnetization within the particle may become ambiguous at a low magnetic field.[18] Perpendicular magnetic and structural orientations are accessible for few materials, including goethite (α-FeO(OH)) rods that align parallel to a small magnetic field below 0.35 T, but re-align at high field with their long axis perpendicular to the applied field due to diamagnetic susceptibility anisotropy.[19–21] Due to strong magnetocrystalline anisotropy above the Morin transition (T_M = 263 K),[22,23] hematite (α-Fe_2O_3) nanospindles are magnetized perpendicular to their long axis and thus align with their short axis along the external field. In order to exploit competing morphological and magnetic orientation towards applications, precise knowledge of the orientation behavior of the magnetic director ($\mathbf{e_A}$) within the particle is indispensable. With this study, we aim to give a detailed account on the orientation of the magnetic moment in hematite nanospindles with respect to both the anisometric particle shape and the crystallographic lattice.

Hematite nanospindles are routinely synthesized[24,25] with the *c* axis of the corundum structure along the long axis of the

[a]*Large Scale Structures group, Institut Laue-Langevin, 71 avenue des Martyrs, F-38042 Grenoble, France*
[b]*Department für Chemie, Universität zu Köln, Luxemburger Strasse 116, D-50939 Köln, Germany. E-mail: sabrina.disch@uni-koeln.de*
[c]*ESRF – The European Synchrotron, 71 avenue des Martyrs, F-38043 Grenoble, France*
[d]*Physics and Materials Science Research Unit, Université du Luxembourg, 162 A, avenue de la Faïencerie, L-1511 Luxembourg, Luxembourg*

†Electronic supplementary information (ESI) available. See DOI: 10.1039/C8NR09583C

‡Present address: Large Scale Structures group, Institut Laue-Langevin, 71 avenue des Martyrs, F-38042 Grenoble, France.

spindle, which is the main rotational axis. The strong magnetocrystalline anisotropy of hematite dominates over the shape anisotropy even at large aspect ratios. In colloidal solution hematite nanospindles exhibit a pseudo-superparamagnetic behavior induced by Brownian motion with a spontaneous magnetization that is typically reached in a low applied magnetic field of few tens of mT.[26] In large magnetic field, the particle long axis is restricted to the plane perpendicular to the applied field.[27,28] The field-dependent alignment of these particles has been described by phenomenological approaches for the orientational distribution function, considering different susceptibilities along and across the particle axis.[29] These approaches allowed the elucidation of the hindrance of magnetic field-alignment resulting from particle–matrix interactions in hydrogels.[30] Boltzmann statistics was considered to describe the magnetic order parameter of silica-coated nanospindles in the applied field.[27] In all previous SAXS studies, the angular orientation distribution was subject to refinement.

Superparamagnetic relaxation of the magnetic moment within the basal plane is possible, whereas high energy is needed to tilt the magnetic moment out of the basal plane.[31] Experimental evidence has been reported for relocation of the magnetization vector within the basal plane of non-interacting nanospindles[27–29] as well as a fixed easy magnetic direction in the basal plane.[32] For hematite nanospindles with arrested orientation by either deposition techniques or incorporation into a gel-like matrix, uniaxial anisotropy is consistently observed.[26,33] However, the morphological particle orientation distribution obtained from the SAXS analysis alone does not discriminate a magnetic easy axis within the basal plane from a magnetic easy plane scenario. Precise knowledge of the moment orientation within anisometric nanoparticles is important for the development of new materials with directional magnetic anisotropies.[34] It is further expected to enhance the understanding of dipolar interactions in nanoparticle assemblies and aggregates. This will be particularly useful in flow environments such as nanorheology or microfluidics, where the competition of steric nanoparticle packing and magnetic dipolar interactions is decisive for the materials performance.[34]

Here we present a combined study of magnetic field-dependent SAXS and WAXS measurements on hematite nanospindles, giving insight into the structural, crystallographic and magnetic orientation. We introduce an approach to fully describe the alignment of anisometric NPs in a magnetic field applied either perpendicular or parallel to the incident beam. The simulation framework is analogously extendable to anisometric particles with different magnetic anisotropies and orientations of the magnetic easy axis. It may also take a numerically calculated angular distribution function as an input, *e.g.* from molecular dynamics simulations for shear aligned systems. For non-interacting NPs in dilute dispersion, we calculate the orientation distribution function based on the Boltzmann statistics, and correlate the magnetic and nematic order parameters. For the evaluation of particle orientation based on the SAXS simulation, the magnetic orientation with respect to the crystal structure is obtained from the magnetic field dependent texture analysis of WAXS data.

2 Materials and methods

2.1 Synthesis

Hematite NPs with spindle shape were synthesized by the hydrolysis method developed by Matijević and co-workers.[24] In brief, aqueous solutions of 70 mL of $FeCl_3$ (26 mmol) and 30 mL of NaH_2PO_4 (0.8047 mmol) were mixed in 1 L of preheated water at 90° C. The reaction was carried out under reflux for 96 h, and the obtained orange dispersion of NPs was purified by five cycles of centrifugation at 7000 rpm for 10 min and redispersion in water. A water suspension with a final concentration of 14 mg mL^{-1} was prepared.

2.2 Characterization

X-ray powder diffraction (XRPD) was measured using a PANalytical X'Pert PRO diffractometer equipped with a secondary monochromator and a PIXcel detector. The sample was dried to a powder and measured on a flat plate glass sample holder in reflection geometry. Data were acquired using Cu K_α radiation (λ = 1.54 Å) over a range of scattering angles 2θ = 5–80° with a step size of 0.03°, corresponding to a Q range of 1–5 $Å^{-1}$. Rietveld analysis was carried out using the FullProf software,[35] applying a pseudo-Voigt profile function. The instrumental broadening was obtained from a LaB_6 reference measurement (SR 660b, NIST).

Transmission Electron Microscopy (TEM) was performed on a ZEISS LEO 902 microscope operating at 120 kV with a LaB_6 cathode in bright field (BF) mode. The sample was deposited onto a coated copper grid. The mean particle diameter was determined from more than 200 particles in different BF images and the histogram was modelled with a log-normal distribution function.

Small-Angle/Wide-Angle X-ray Scattering (SAXS/WAXS) measurements were done simultaneously in an applied magnetic field using the ID02 instrument (ESRF) at a wavelength of λ = 0.995 Å. The SAXS data were collected on a Rayonix MX-170HS CCD detector placed inside an evacuated 34 m detector tube at two sample–detector distances of 30 and 1.5 m, and the WAXS data were acquired by using a Rayonix LX-170HS CCD detector in air at a distance of 0.137 m from the sample position. Aqueous dispersions of hematite NPs were sealed air-tight in quartz capillaries, and scattering experiments were performed in a static magnetic field up to 520 mT, applied either perpendicular or parallel to the incoming beam, with the total length of the beam path in air being 0.24 m. SAXS data were normalized to detector efficiency, capillary thickness, transmission, and background and calibrated to absolute scattering intensity using water as the reference material. The SAXS data measured at the short sample–detector distance were scaled to overlap with those measured at the long sample–detector distance in order to correct for a maximum 5% deviation in scattering intensity, most likely

originating in a small degree of sedimentation of the particles between the measurements. WAXS 2D data were polarization corrected and 1D data were corrected to transmission, capillary thickness and background. Starting with 120 mT, the Halbach magnet setup (Fig. S1†) shadows the WAXS detector at the corner. For this reason, WAXS measurements at higher fields have been excluded from further analysis.

Vibrating Sample Magnetometry (VSM) measurements were performed on an ADE EV7 Magnetics Vibrating Sample Magnetometer (VSM). The dilute NP dispersion was sealed in a Teflon crucible and placed on a glass sample holder. Room temperature (298 K) magnetization data were collected in a field range ±2.2 T with a head drive frequency of 75 Hz.

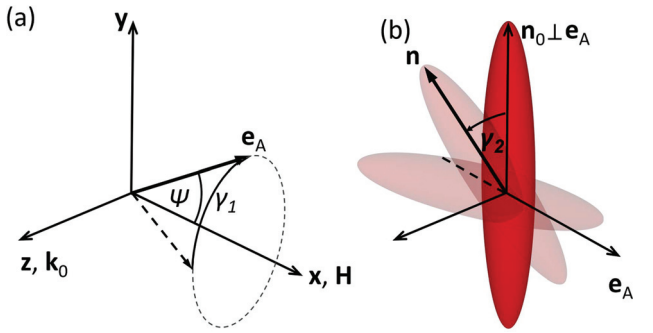

Fig. 1 (a) Laboratory coordinate system introducing the angles ψ and γ_1 of the easy axis orientation $\mathbf{e_A}$ with respect to the applied magnetic field H and (b) the particle coordinate system with the polar particle axis **n** oriented perpendicular to the easy axis with a precession angle γ_2 between **n** and $\mathbf{n_0}$.

3 Model

To simulate the SAXS pattern of hematite nanospindles with a given orientation distribution, we apply the form factor of an ellipsoid of revolution. The form factor amplitude $K(Q, \alpha)$ is defined as[36]

$$K(Q,\alpha) = \frac{3\sin(QR) - qR\cos(QR)}{(QR)^3} \quad (1)$$

$$R = \sqrt{{R_0}^2 \cdot \sin^2\alpha + {R_L}^2 \cdot \cos^2\alpha}, \quad (2)$$

where R_0 is the equatorial radius and R_L is the polar radius of the ellipsoid. However, as our definition of the projection angle α of the polar axis **n** towards the scattering vector **Q** on the detector plane x–y is independent of the chosen form factor, other anisometric form factors, such as a cylinder, can be introduced.

In the following, the field-induced orientation distribution of the projection angle α will be derived for anisometric NPs with the structural main axis and magnetization both perpendicular to each other. The magnetic moment of a NP with sufficiently large magnetocrystalline anisotropy compared to thermal energy is oriented in the magnetic easy direction of the material. For freely dispersed NPs (Newtonian fluid), the application of a static magnetic field will not change the average orientation of the particle moment along the easy direction, as Brownian motion enables the particle to rotate in the energetically most favored orientation. The orientation of the easy axis $\mathbf{e_A}$ with respect to the applied field **H** is described in a spherical coordinate system with a polar angle ψ towards the applied magnetic field and a precession angle γ_1 (Fig. 1a).

The easy axis orientation $\mathbf{e_A}$ is thus given by:

$$\mathbf{e_A} = \begin{pmatrix} \cos\psi \\ \sin\psi \cdot \sin\gamma_1 \\ \sin\psi \cdot \cos\gamma_1 \end{pmatrix}. \quad (3)$$

In the case of hematite, the easy axis is located in the basal plane, corresponding to the equatorial plane of the anisometric NP. An arbitrary orientation $\mathbf{n_0}$ of the particle polar axis with respect to the easy axis, as shown in Fig. 1b, is given as

$$\mathbf{n_0} = \begin{pmatrix} -\sin\psi \\ \cos\psi \cdot \sin\gamma_1 \\ \cos\psi \cdot \cos\gamma_1 \end{pmatrix}. \quad (4)$$

The description of all possible orientations in the plane perpendicular to $\mathbf{e_A}$ with a precession angle γ_2 can be found with

$$\mathbf{n} = \mathbf{n_0} \cdot \cos\gamma_2 + (\mathbf{n_0} \times \mathbf{e_A})\sin\gamma_2. \quad (5)$$

The projection angle α of the polar axis **n** to the scattering vector **Q** on the detector plane (Q_x, Q_y) is obtained with

$$\cos\alpha = \mathbf{n} \cdot \frac{\mathbf{Q}}{Q}. \quad (6)$$

Finally, the particle form factor $F(Q)$ of an oriented particle ensemble is calculated according to

$$F(Q) = \frac{1}{4\pi^2}\int_0^{2\pi} d\gamma_2 \int_0^{2\pi} d\gamma_1 \int_0^{\pi} d\psi \, \sin\psi P(\psi) K(Q,\alpha)^2, \quad (7)$$

where $K(Q, \alpha)$ is the form factor amplitude, which is given by eqn (1) for an ellipsoid of revolution. We assume free particle precession in dispersion, *i.e.* isotropic distribution of γ_1 and γ_2. The angular distribution $P(\psi)$ of the easy axis $\mathbf{e_A}$ towards the applied magnetic field direction follows Boltzmann statistics according to

$$P(\psi) = \frac{\xi \exp(\xi\cos\psi)}{\exp(\xi) - 1}, \quad (8)$$

with the Langevin parameter $\xi = \frac{\mu\mu_0 H}{k_B T}$. Here, μ_0 is the permeability of free space, μ is the integral particle moment, k_B is the Boltzmann constant, and T is the absolute temperature. This approach directly connects experimental parameters, *i.e.* the particle moment, the applied magnetic field and temperature, to the orientation distribution and hence allows simulating the corresponding SAXS cross section.

Different order parameters have traditionally been used to describe magnetically induced orientation and anisotropic shape. The Langevin function represents the first moment of the orientation distribution according to $S_1 = \langle \cos \psi \rangle$ (*cf. e.g.* eqn (10)). It can be considered as the magnetic order parameter, relating the average orientation of the magnetic easy axis towards the applied field and ranges from $S_1(H = 0) = 0$ for the isotropic case to $S_1(H \to \infty) = 1$ for perfect alignment. Regarding the structural order, the second moment of the orientation distribution according to $S_2 = \frac{1}{2}\langle 3\cos^2(\omega) - 1 \rangle$ is conventionally applied to describe the nematic order induced in anisometric colloids. The easy axis order parameter $S_{2,\mathbf{e_A}}$ considers the magnetic easy axis $\mathbf{e_A}$ as the director ($\omega = \psi$) and $S_{2,\mathrm{n}}$ considers the polar particle axis $\mathbf{n}$ as the director ($\omega = \omega_\mathrm{n}$). Both equivalent notations are used in the literature and we provide both quantities for comparative reasons. For the latter case, the angle ω_n between polar particle axis $\mathbf{n}$ and applied magnetic field direction x is derived according to

$$\cos \omega_\mathrm{n} = \mathbf{n} \cdot \begin{pmatrix} 1 \\ 0 \\ 0 \end{pmatrix}. \quad (9)$$

In Fig. 2, the nematic order parameters are shown and compared to the Langevin function for our example of hematite nanospindles. Both magnetic order parameters, S_1 and $S_{2,\mathbf{e_A}}$, increase with increasing applied field, *i.e.* from isotropic distribution at zero field (S_1, $S_{2,\mathbf{e_A}} = 0$) to the fully ordered state (S_1, $S_{2,\mathbf{e_A}} = 1$), albeit with a different slope as they are related to the first and second moments of the orientation distribution, respectively. The nematic order parameter $S_{2,\mathrm{n}}$ approaches $S_{2,\mathrm{n}} = -0.5$ for perfect alignment of the magnetic easy axis, as the particle director will be aligned perpendicular to the applied field. Consequently, the nematic order parameters are related by $S_{2,\mathrm{n}} = -1/2\ S_{2,\mathbf{e_A}}$.

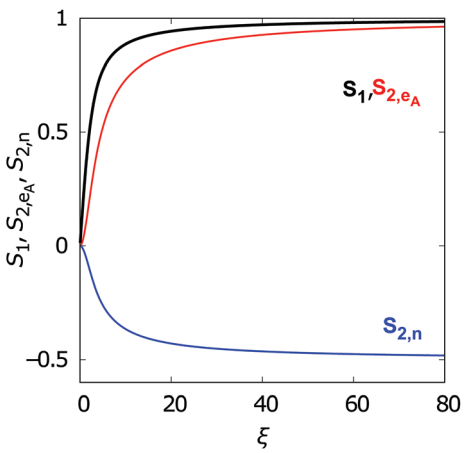

Fig. 2 Comparison of Langevin function (S_1) and nematic order parameters relating to the magnetic easy axis ($S_{2,\mathbf{e_A}}$) and the polar particle axis ($S_{2,\mathrm{n}}$) as the particle director.

4 Results and discussion

For our combined SAXS/WAXS study, hematite nanospindles with a large aspect ratio were prepared by established synthesis routes.[24] The spindle-like morphology is confirmed by TEM data (Fig. 3a) revealing a particle length of 375(14) nm (σ_log = 19.1%) and a diameter of 56(2) nm (σ_log = 18.7%). The corresponding aspect ratio of 6.7(1) is in the larger limit of aspect ratios obtainable by this synthesis approach.[24] A particle volume of $V_\mathrm{TEM} = 5.0(3) \times 10^{-22}$ m^3 is determined according to the spindle shape.[29] XRPD of the dried sample confirms the pure hematite phase (Fig. 3b) with rhombohedral lattice parameters $a = b = 5.031(1)$ Å, $c = 13.814(1)$ Å (space group $R\bar{3}c$), which is in good agreement with bulk lattice parameters, $a = b = 5.038(1)$ Å, $c = 13.772(1)$ Å.[37] Using spherical harmonics[38] in Rietveld refinement leads to the coherent domain sizes of 73 (1) nm, 47(2) nm, and 288(3) nm for the (1 0 4), (1 1 0), and (0 0 6) reflection, respectively (for more information see Fig. S2†). The crystalline coherent domain size is in general good agreement with the obtained size of 56(2) nm for the spindle diameter obtained using TEM with a considerably larger coherent domain size along the crystallographic c direction.

The particle morphology is confirmed by the analysis of the isotropic small-angle X-ray scattering (SAXS) obtained in a zero applied field (Fig. 3c). Applying the form factor of an ellipsoid of revolution and assuming isotropic distribution, the length $l = 326(1)$ nm (σ_log = 15%) and diameter $d = 54(1)$ nm (σ_log = 15%) are obtained, which corresponds to a particle volume of

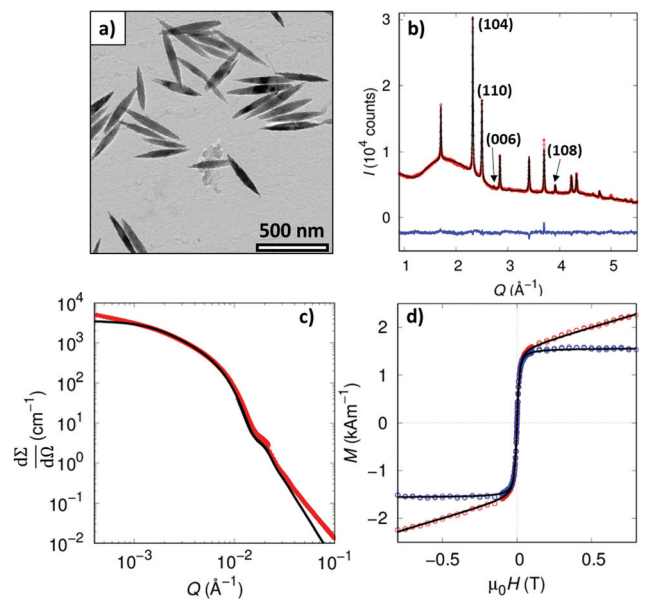

Fig. 3 (a) TEM bright field micrograph. (b) Rietveld refinement (black line) of XRPD data (red points), the blue line corresponds to the residuals and vertical green lines denote Bragg's maxima of $R\bar{3}c$. (c) Isotropic SAXS data (red points) with the ellipsoidal form factor fit (black line). (d) Isothermal magnetization curve with (red points) and without (blue points) excess paramagnetic susceptibility, together with the Langevin fit (black line).

V_{SAXS} = 5.0(1) × 10^{-22} m^3. Whereas the determined diameter and volume are in excellent agreement with the TEM evaluation, the considerably shorter particle length observed by SAXS compared to TEM is understood as a result of the non-perfect description of a spindle-type particle with an ellipsoid of revolution. Indeed, the SAXS data presented in Fig. 3c reveal a slight increase in scattering intensity in the lower and upper Q range, which might be attributed to a small structure factor contribution and to the deviation of the particle shape from a perfect ellipsoid, respectively. For the description of SAXS by nanospindles, the precise spindle form factor was reported.[29] However, to maintain reasonable computing times for our orientation distribution model, the simpler ellipsoid of revolution is applied here. This is justified by the excellent agreement of data and simulation in the Q range relevant for analysis of the orientation distribution (Q = 0.004–0.03 $Å^{-1}$).

Magnetization measurements reveal a combination of two individual contributions, *i.e.* a Langevin-type magnetization contribution and an excess magnetic susceptibility observed up to a large applied field (Fig. 3d). The Langevin-type behavior is typically observed for magnetic NPs in dispersion, and related to Brownian rotation of the magnetically blocked NPs towards the applied magnetic field. It is therefore relevant for the orientation distribution of anisometric NPs. Excess magnetic susceptibility is commonly attributed to spin disorder. In the case of hematite it is also observed as a result of exchange between the magnetic sublattices.[32] As this contribution is intrinsic to the NPs and not related to the particle orientation in the applied magnetic field, only the Langevin-type contribution has to be considered for the description of the particle orientation distribution function. The magnetization data are corrected for the excess susceptibility and refined to the Langevin-type behavior scaled by the spontaneous magnetization σ_s according to

$$\sigma_s \mathscr{L}(\xi) = \sigma_s \left(\coth \xi - \frac{1}{\xi} \right). \quad (10)$$

The Langevin function $\mathscr{L}(\xi)$ is identical to S_1. An integral particle moment of μ = 6.6(1) × 10^{-19} J T^{-1}, corresponding to 7.1(1) × $10^4 \mu_B$, is obtained along with a spontaneous magnetization of σ_s = 1566(1) A m^{-1}. The spontaneous magnetization corresponds to 78.3% of the bulk value for hematite of 2000 A m^{-1},[32] which is in agreement with previous reports.[26,28] The integral particle moment relates to a magnetic particle volume of $V_{mag} = \mu/\sigma_s$ = 4.2(1) × 10^{-22} m^3, which is significantly smaller than the morphological particle volume, V_{TEM} = 5.0(3) × 10^{-22} m^3 and V_{SAXS} = 5.0(1) × 10^{-22} m^3, as obtained from TEM and SAXS analysis, respectively. A reduced magnetic particle volume is commonly observed for magnetic NPs and attributed to enhanced spin disorder towards the particle surface. Already a slightly smaller equatorial diameter of 47(2) nm, as derived for the structurally coherent grain size from XRPD analysis, leads to a significantly smaller particle volume. The magnetically coherent particle volume determined from VSM measurements here is thus reasonable for a single-domain NP with enhanced surface spin disorder.

SAXS data of the nanospindle dispersion under an applied magnetic field are presented in Fig. 4a. Without the applied field, the 2D SAXS pattern is isotropic and corresponds to the randomly oriented particle ensemble. The elongation of the scattering pattern parallel to the applied field corresponds to a preferential orientation of the long (polar) axis perpendicular to the applied field.

Application of a magnetic field parallel to the incoming X-ray beam results in a scattering pattern that remains isotropic, but reveals a decreasing scattering intensity with increasing magnetic field. This confirms free particle rotation in the plane perpendicular to the applied field (Fig. S3†).

To simulate the anisotropic SAXS patterns presented in Fig. 4, we use the morphological parameters and particle volume concentration determined from the isotropic SAXS experiment and the integral particle moment by VSM. Comparison of the experimental scattering data and simulated 2D patterns for different applied fields suggests good agreement between the simulated and the real particle orientation distribution in dispersion.

The anisotropy of the scattering pattern is clearly visible in the azimuthal scattering intensity presented in Fig. 5. Field-dependent azimuthal scattering intensities obtained for a selected Q = 0.004 $Å^{-1}$ reveal an excellent agreement between data and simulation at different applied magnetic fields (Fig. 5a). Exemplarily, for the scattering pattern measured at the highest applied field of 520 mT, the azimuthal scattering intensity data confirm the excellent agreement with our simulation over a wide Q range (Fig. 5b). Sector analysis of the 2D scattering data and simulation in horizontal (κ = 0°) and vertical (κ = 90°) directions is presented in Fig. 6. In both cases, we observe a good agreement between data and simulation for all applied fields. The small discrepancy visible in the horizontal sector at Q = 0.001–0.0035 $Å^{-1}$ is attributed to the non-perfect particle shape, *i.e.* simulation of an ellipsoidal as opposed to a spindle-like form factor, as already discussed in section 3. The vertical scattering intensity is less sensitive to field variation, as expected from the azimuthal scattering shown in Fig. 5. It

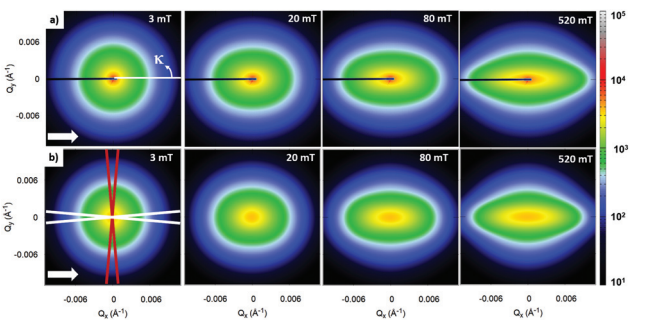

Fig. 4 Comparison of the (a) SAXS data and (b) simulations for a horizontally applied magnetic field $\mu_0 H$ (white arrows). Sectors for integration around an azimuthal angle of κ = 0° and κ = 90° are marked with white and red lines, respectively.

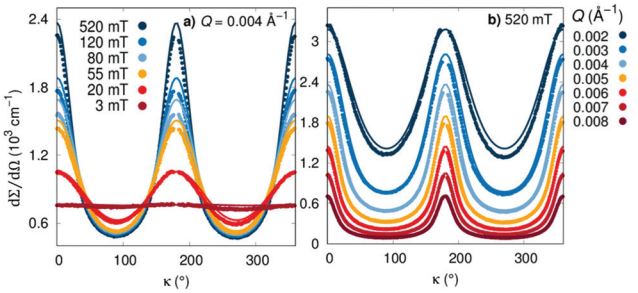

Fig. 5 (a) Field-dependent azimuthal scattering intensity at Q = 0.004 Å^{-1}. (b) Azimuthal scattering intensity for different Q-values in an applied magnetic field of 520 mT (experimental data are presented by dots and simulation by full lines).

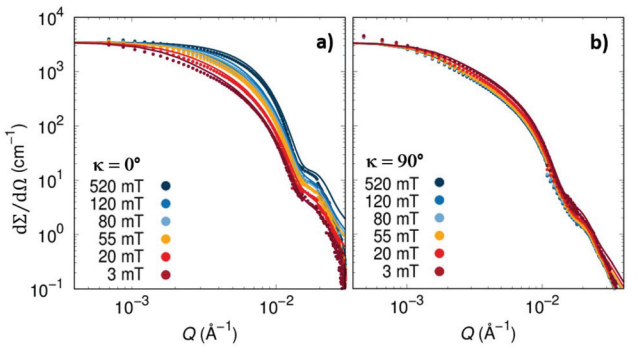

Fig. 6 Comparison of 1D data (points) with simulation (full lines) of 10° wide sectors around (a) κ = 0° and (b) κ = 90°.

reveals a small structure factor contribution, visible as a slight intensity increase at lowest Q, which is not taken into account by our simulations. Such a structure factor indicates a small volume fraction of agglomeration of the spindles. Soft agglomeration may be caused by directional dipole–dipole interactions,[39–42] which are present in anisometric particles depending on the particle moment and mean interparticle distance and may eventually lead to the particle assemblies.[43,44] A variety of different ground states and field-induced particle arrangements has been reported.[42,43,45–47] However, as the observed structure factor is very small and independent of the applied field (see Fig. S4 in the ESI†), we conclude that dipolar interactions in our sample are negligible.

The orientation of the atomic crystal lattice is accessible using WAXS texture analysis. This allows the discrimination between easy axis and easy plane anisotropy of magnetization within the basal plane. 2D WAXS patterns are shown in Fig. 7a and b. Next to broad scattering contributions (Q-range of 1.5–1.7 Å^{-1}) resulting from the solvent, sharp Debye–Scherrer rings are observed, corresponding to the hematite crystal structure. At high magnetic field the texture of Bragg reflections is clearly visible giving direct information on the crystallographic orientation of nanospindles in aqueous dispersion. With an increasing applied field, (1 0 4) and (0 0 6) reflections, which correspond to the lattice planes (preferentially) along the polar

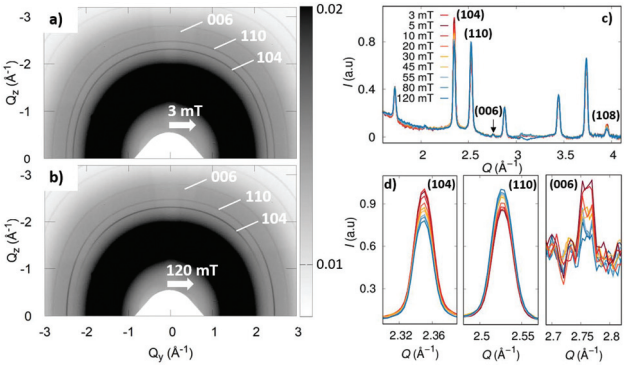

Fig. 7 2D WAXS data in applied magnetic fields of (a) 3 mT and (b) 120 mT (white arrows indicate the direction of the applied magnetic field). (c) Field dependence of the radially integrated WAXS pattern. (d) Magnification of (1 0 4), (1 1 0) and (0 0 6) reflections.

spindle axis, are pronounced in the vertical direction of the 2D image. This is in agreement with the alignment of the long spindle axis perpendicular to the applied magnetic field. The radially averaged data over κ = 0–180° reveal intensity changes with the applied magnetic field for all reflections (Fig. 7c). The integrated scattering intensity decreases for reflections near the hematite c direction ((1 0 4), (1 0 8), (0 0 6)) and concomitantly increases with field strength for reflections within the basal plane (1 1 0) with field strength (for more detailed information see Fig. S5†). The azimuthal scattering intensity of the (1 1 0) reflection gives quantitative information on the field-induced orientation of the crystal lattice (Fig. 8a). A strong texture of the (1 1 0) reflection is observed at κ = 0° and 180°. From the WAXS texture we can extract the structural order parameter according to

$$S = \frac{1}{2} \cdot \left(3 \frac{\int_0^{2\pi} I(\kappa) \cos^2 \kappa \mathrm{d}\kappa}{\int_0^{2\pi} I(\kappa)} - 1 \right). \quad (11)$$

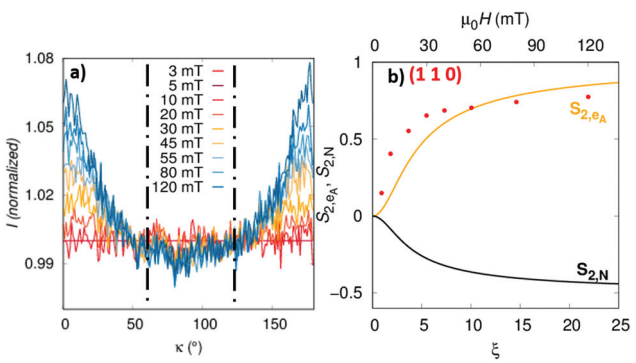

Fig. 8 (a) Azimuthal-angle dependence of the WAXS intensity of (1 1 0) reflection (dashed lines representing the theoretical position of the texture at 60 and 120°). (b) Comparison of the field induced order parameter of the (1 1 0) reflection obtained from WAXS analysis (red dots) with order parameters obtained from magnetometry (grey and orange lines).

The derived order parameter for the (1 1 0) lattice plane presented in Fig. 8b is in reasonable agreement with the morphological order parameter $S_{2,\mathbf{e}_A}$, which we obtained from SAXS simulations. The observed deviations are attributed to the different weightings depending on the applied technique.[48,49] Intensity-weighted techniques such as SAXS and WAXS tend to overestimate larger particles as compared to number-weighted TEM and volume-weighted magnetometry. Therefore, the order parameter derived from WAXS analysis increases faster than the one simulated from Langevin behavior.

The WAXS texture of the (1 1 0) reflection gives additional insight into the easy axis orientation within the hematite basal plane. For a fixed orientation of the magnetic easy axis in the basal plane, a strong texture at intervals of 60° is expected due to the hexagonal symmetry of the hematite crystal structure. As this symmetry is absent from the azimuthal scattering intensities, we surmise that the magnetic moment fluctuates due to thermal activation around the fixed easy axis direction within the basal plane. A similar, quantitative evaluation of the texture in the hematite *c* direction is desirable, but not accessible from our data due to the low intensity of the (0 0 6) reflection (Fig. 7c). Due to its significant deviation from the crystallographic *c* axis, the texture of the (1 0 4) reflection is not directly correlated to the order parameter of the particle. The pronounced scattering intensity in the sector perpendicular to the applied field, however, agrees qualitatively with the orientation of the polar particle axis perpendicular to the field direction (Fig. S6†).

5 Conclusion

We have analyzed the orientation behavior of anisometric magnetic NPs in an applied magnetic field using SAXS and WAXS measurements. The 2D SAXS pattern is simulated based on information on morphological details, particle number density and the integral NP moment obtained from pre-characterization methods, without varying any free fit parameters. The alignment in magnetic field is described by a Boltzmann distribution and hence Langevin-like behaviour of the easy axis inclination angle. In principle, the formalism allows the implementation of any particle shape with prolate or oblate symmetry and orientation behavior of the magnetic easy direction either parallel or perpendicular to the polar particle axis. We demonstrate that our simulations coincide well with the experimental results for the case of spindle-shaped hematite NPs. The excellent agreement between experiment and simulation supports the assumption that the easy axis lies always in the equatorial particle direction. Texture analysis of the WAXS data further confirms that the magnetic easy axis is located in the basal plane of the hematite crystal structure. In consequence, the crystallographic *c* axis of the single-crystalline nanospindles is parallel to the long particle axis. Moreover, the WAXS results confirm the tendency for uniaxial anisotropy, however, with strong thermal fluctuation of the magnetic moment within the basal plane.

Our combined study of the orientation behavior on both atomic and colloidal scales thus gives detailed insight into the orientation of magnetization with respect to the magnetic easy direction in the crystal lattice and the morphological orientation of the spindles in the applied magnetic field. These results highlight hematite nanospindles as a model system to characterize orientational situations using either SAXS, WAXS or macroscopic magnetization measurements. Understanding the magnetization direction in anisometric NPs is important for the development of new smart materials and has the potential to enhance application in the field of nanorheology, microfluidic devices such as micro-stirrers, or in the field of sensors.

Conflicts of interest

There are no conflicts to declare.

Acknowledgements

This work is based on experiments performed at the ID02 beamline at the European Synchrotron Radiation Facility (ESRF), Grenoble, France. We thank Daniel Nižňanský for X-ray diffraction measurements performed at Charles University in Prague, Czech Republic. We also thank Stefan Roitsch for the acquisition of TEM micrographs. Financial support from the German Research Foundation (DFG: Emmy Noether Grant DI 1788/2-1) is gratefully acknowledged.

References

1 Q. A. Pankhurst, J. Connolly, S. K. Jones and J. Dobson, *J. Phys. D: Appl. Phys.*, 2003, **36**, R167.
2 B. Tian, Z. Qiu, J. Ma, M. Donolato, M. F. Hansen, P. Svedlindh and M. Strömberg, *ACS Appl. Mater. Interfaces*, 2018, **10**, 2957–2964.
3 I. Nándori and J. Rácz, *Phys. Rev. E: Stat., Nonlinear, Soft Matter Phys.*, 2012, **86**, 061404.
4 D. T. Chen, Q. Wen, P. A. Janmey, J. C. Crocker and A. G. Yodh, *Annu. Rev. Condens. Matter Phys.*, 2010, **1**, 301–322.
5 J. Connolly and T. G. S. Pierre, *J. Magn. Magn. Mater.*, 2001, **225**, 156–160.
6 A. Tschöpe, K. Birster, B. Trapp, P. Bender and R. Birringer, *J. Appl. Phys.*, 2014, **116**, 184305.
7 E. Roeben, L. Roeder, S. Teusch, M. Effertz, U. K. Deiters and A. M. Schmidt, *Colloid Polym. Sci.*, 2014, **292**, 2013–2023.
8 P. Bender, A. Günther, D. Honecker, A. Wiedenmann, S. Disch, A. Tschöpe, A. Michels and R. Birringer, *Nanoscale*, 2015, **7**, 17122–17130.
9 J. A. N. Zasadzinski and R. B. Meyer, *Phys. Rev. Lett.*, 1986, **56**, 636–638.
10 A. van Blaaderen, M. Dijkstra, R. van Roij, A. Imhof, M. Kamp, B. W. Kwaadgras, T. Vissers and B. Liu, *Eur. Phys. J.: Spec. Top.*, 2013, **222**, 2895–2909.

11 A. Ahniyaz, Y. Sakamoto and L. Bergström, *Proc. Natl. Acad. Sci. U. S. A.*, 2007, **104**, 17570–17574.
12 A. B. D. Brown, C. Ferrero, T. Narayanan and A. R. Rennie, *Eur. Phys. J. B*, 1999, **11**, 481–489.
13 T. H. Besseling, M. Hermes, A. Fortini, M. Dijkstra, A. Imhof and A. van Blaaderen, *Soft Matter*, 2012, **8**, 6931–6939.
14 P. Bender, A. Tschöpe and R. Birringer, *J. Magn. Magn. Mater.*, 2014, **372**, 187–194.
15 P. Bender, F. Krämer, A. Tschöpe and R. Birringer, *J. Phys. D: Appl. Phys.*, 2015, **48**, 145003.
16 G. Armelles, A. Cebollada, A. García-Martín, J. M. Montero-Moreno, M. Waleczek and K. Nielsch, *Langmuir*, 2012, **28**, 9127–9130.
17 J. Bachmann, J. Jing, M. Knez, S. Barth, H. Shen, S. Mathur, U. Gösele and K. Nielsch, *J. Am. Chem. Soc.*, 2007, **129**, 9554–9555.
18 L. G. Vivas, R. Yanes and A. Michels, *Sci. Rep.*, 2017, **7**, 13060.
19 B. J. Lemaire, P. Davidson, J. Ferré, J. P. Jamet, P. Panine, I. Dozov and J. P. Jolivet, *Phys. Rev. Lett.*, 2002, **88**, 125507.
20 H. H. Wensink and G. J. Vroege, *Phys. Rev. E: Stat., Nonlinear, Soft Matter Phys.*, 2005, **72**, 031708.
21 G. J. Vroege and H. N. W. Lekkerkerker, *Rep. Prog. Phys.*, 1992, **55**, 1241.
22 I. Dzyaloshinsky, *J. Phys. Chem. Solids*, 1958, **4**, 241–255.
23 A. H. Morrish, *Canted antiferromagnetism: Hematite*, World Scientific Publishing Co. Pte. Ltd., 1994.
24 M. Ozaki, S. Kratohvil and E. Matijević, *J. Colloid Interface Sci.*, 1984, **102**, 146–151.
25 T. Sugimoto, A. Muramatsu, K. Sakata and D. Shindo, *J. Colloid Interface Sci.*, 1993, **158**, 420–428.
26 D. Hoffelner, M. Kundt, A. M. Schmidt, E. Kentzinger, P. Bender and S. Disch, *Faraday Discuss.*, 2015, **181**, 49–461.
27 M. Reufer, H. Dietsch, U. Gasser, A. Hirt, A. Menzel and P. Schurtenberger, *J. Phys. Chem. B*, 2010, **114**, 4763–4769.
28 M. Reufer, V. A. Martinez, P. Schurtenberger and W. C. K. Poon, *Langmuir*, 2012, **28**, 4618–4624.
29 C. Märkert, B. Fischer and J. Wagner, *J. Appl. Crystallogr.*, 2011, **44**, 441–447.
30 A. Nack, J. Seifert, C. Passow and J. Wagner, *J. Appl. Crystallogr.*, 2018, **51**, 87–96.
31 W. O'Reilly, *Rock and Mineral Magnetism*, Springer, US, 1984.
32 F. Bødker, M. F. Hansen, C. B. Koch, K. Lefmann and S. Mørup, *Phys. Rev. B: Condens. Matter Mater. Phys.*, 2000, **61**, 6826–6838.
33 L. Roeder, P. Bender, M. Kundt, A. Tschöpe and A. M. Schmidt, *Phys. Chem. Chem. Phys.*, 2015, **17**, 1290–1298.
34 P. Tierno, *Phys. Chem. Chem. Phys.*, 2014, **16**, 23515–23528.
35 J. Rodríguez-Carvajal, *Physica B*, 1993, **192**, 55.
36 L. Feigin and D. I. Svergun, *Structure Analysis by Small-Angle X-ray and Neutron Scattering*, Princeton Resources, Princeton, 1987.
37 M. C. Morris, H. F. McMurdie, E. H. Evans, B. Paretzkin, H. S. Parker, W.-N. Wong and D. M. Gladhill, *Standard X-ray Diffraction Powder Patterns*, Washington, DC, 1985.
38 M. Järvinen, *J. Appl. Crystallogr.*, 1993, **26**, 525–531.
39 A. Perera and G. N. Patey, *J. Chem. Phys.*, 1989, **91**, 3045–3055.
40 G. Zarragoicoechea, D. Levesque and J. Weis, *Mol. Phys.*, 1991, **74**, 629–637.
41 R. Berardi, S. Orlandi and C. Zannoni, *Int. J. Mod. Phys. C*, 1999, **10**, 477–484.
42 R. Berardi, S. Orlandi and C. Zannoni, *Phys. Chem. Chem. Phys.*, 2000, **2**, 2933–2942.
43 S. Kantorovich, E. Pyanzina and F. Sciortino, *Soft Matter*, 2013, **9**, 6594–6603.
44 T. K. Bose and J. Saha, *Phys. Rev. E: Stat., Nonlinear, Soft Matter Phys.*, 2014, **89**, 046502.
45 M. Yan, J. Fresnais and J.-F. Berret, *Soft Matter*, 2010, **6**, 1997–2005.
46 A. Gil-Villegas, S. C. McGrother and G. Jackson, *Chem. Phys. Lett.*, 1997, **269**, 441–447.
47 D. Levesque, J. J. Weis and G. J. Zarragoicoechea, *Phys. Rev. E: Stat. Phys., Plasmas, Fluids, Relat. Interdiscip. Top.*, 1993, **47**, 496–505.
48 P. Bender, C. Balceris, F. Ludwig, O. Posth, L. K. Bogart, W. Szczerba, A. Castro, L. Nilsson, R. Costo, H. Gavilán, D. González-Alonso, I. de Pedro, L. F. Barquín and C. Johansson, *New J. Phys.*, 2017, **19**, 073012.
49 C. E. Kril and R. Birringer, *Philos. Mag. A*, 1998, **77**, 621–640.